Plasma Chemistry and Plasma Processing (2023) 43:635–656
https://doi.org/10.1007/s11090-023-10320-3

ORIGINAL PAPER

SF_6 Degradation in a γ-Al_2O_3 Packed DBD System: Effects of Hydration, Reactive Gases and Plasma-Induced Surface Charges

Zhaolun Cui[1,2] · **Chang Zhou**[3] · **Amin Jafarzadeh**[2] · **Xiaoxing Zhang**[3] · **Yanpeng Hao**[1] · **Licheng Li**[1] · **Annemie Bogaerts**[2]

Received: 25 April 2022 / Accepted: 30 October 2022 / Published online: 10 April 2023

Abstract

Packed-bed DBD (PB-DBD) plasmas hold promise for effective degradation of greenhouse gases like SF_6. In this work, we conducted a combined experimental and theoretical study to investigate the effect of the packing surface structure and the plasma surface discharge on the SF_6 degradation in a γ-Al_2O_3 packing DBD system. Experimental results show that both the hydration effect of the surface (upon moisture) and the presence of excessive reactive gases in the plasma can significantly reduce the SF_6 degradation, but they hardly change the discharge behavior. DFT results show that the pre-adsorption of species such as H, OH, H_2O and O_2 can occupy the active sites (Al_{III} site) which negatively impacts the SF_6 adsorption. H_2O molecules pre-adsorbed at neighboring sites can promote the activation of SF_6 molecules and lower the reaction barrier for the S-F bond-breaking process. Surface-induced charges and local external electric fields caused by the plasma can both improve the SF_6 adsorption and enhance the elongation of the S-F bonds. Our results indicate that both the surface structure of the packing material and the plasma surface discharge are crucial for SF_6 degradation performance, and the packing beads should be kept dry during the degradation. This work helps to understand the underlying mechanisms of SF_6 degradation in a PB-DBD system.

Keywords SF_6 · DBD treatment · Hydration effect · Reactive gases · Plasma-induced surface charges

---

Zhaolun Cui and Chang Zhou are the authors contributed equally to this paper.

✉ Yanpeng Hao
yphao@scut.edu.cn

Extended author information available on the last page of the article

Introduction

Sulfur hexafluoride (SF_6) is a colorless, odorless, and non-toxic gas with great stability [1, 2]. It shows an excellent dielectric property and has been widely used in the power industry since the 1940s [3, 4]. However, SF_6 is a greenhouse gas with a very high global warming potential (GWP), about 23,500 times that of CO_2 [5]. In 2010, the global emission of SF_6 raised to 5.31 Gg (gigagram), with an average annual growth rate of about 10% [6]. In 2015–2040, the global electricity demand is expected to grow by 30%, which could further increase the detrimental effects of SF_6 on the environment [7, 8].

Since the end of the last century, great efforts have been devoted to the abatement of SF_6 waste gases. However, the SF_6 molecule has stable S-F bonds and is hard to decompose, and the incompletely decomposed intermediates (SF_x, $x < 6$) can easily recombine again with F atoms into SF_6, as shown in Eq. 1 [9].

$$SF_x + (6 - x)F \rightarrow SF_6 \tag{1}$$

Due to these properties, the effective degradation of SF_6 needs some additional conditions. Therefore, methods like thermal degradation [1], thermal catalysis, photocatalysis, electrocatalysis, and non-thermal plasma (NTP) have been applied for this purpose [1, 10–15]. Among them, NTP shows promising performance for SF_6 abatement, both in terms of degradation efficiency and energy yields, by means of various plasma types, such as dielectric barrier discharge (DBD), microwave discharge, and radio-frequency discharge [16–20]. Often, reactive gases, like H_2, O_2, or H_2O, are added in the NTP treatment to improve the degradation efficiency [9, 21]. However, the results show a lack of product selectivity without employing a suitable catalyst [15]. Therefore, we used a packed-bed DBD (PB-DBD) for SF_6 treatment and found that a packing of glass beads, as well as γ-Al_2O_3 beads, promoted the discharge and the degradation process [22]. Moreover, the γ-Al_2O_3 packing shows an ability for the activation of SF_6 and the regulation of its degradation products due to its surface properties [23], which prove that γ-Al_2O_3 is a proper packing material for SF_6 treatment in a DBD system.

It should be noted that the surface properties of the catalyst are of great importance for its performance [24]. γ-Al_2O_3 has an active surface and an adsorption ability, making it a good catalyst support. During a long-term use, γ-Al_2O_3 beads often face the problem of moisture, and the dry surface will be hydrated after the adsorption of H_2O, which may affect the discharge and degradation process [25, 26]. Furthermore, the addition of reactive gases, such as H_2O, O_2, H_2, etc., which is often done in practice to improve the degradation efficiency in the plasma phase (see above), may lead to changes in the surface state of the γ-Al_2O_3 packing and reduce its ability to adsorb and activate the SF_6 molecules [27]. In addition, during the discharge, the plasma may cause excess electrons or an external electric field on the packing material surface, which in a way affect the surface reactions [24]. However, these factors have not been investigated yet, but are vital for understanding the SF_6 degradation mechanism over the packing material surface.

In recent years, plasma catalysis has been successfully applied in various fields [24], like CO_2 conversion [28], CH_4 reforming [29] and VOC treatments [30]. Density functional theory (DFT) has been widely applied to study plasma-catalytic systems in order to provide an atomistic point of view on the underlying mechanisms between the plasma and catalyst [31, 32]. For example, Bal et al. studied the adsorption and activation process of CO_2 molecules on supported M/γ-Al_2O_3 (M is a single metal atom) surface and demonstrated a catalytic effect of this surface upon plasma charging [33]. Shirazi et al. conducted a DFT study to investigate the dry reforming of CH_4 on a Ni surface, to reveal the formation mechanism of the key products and the effects of the pre-adsorbed species [34]. In this regard, DFT simulations are an effective way to study the surface reactions of SF_6 in a PB-DBD plasma-catalytic system.

In this study, we conducted experiments and DFT calculations to investigate the effects of the surface structure of the γ-Al_2O_3 packing and the plasma surface discharge on SF_6 degradation. The hydration, excessive addition of reactive gases (H_2O and O_2), plasma-induced surface charges and external electric fields are proved to be effective factors in determining the degradation performance. This work provides experimental results, backed up by theoretical explanations, for a better understanding of SF_6 decomposition on different kinds of γ-Al_2O_3 surface structures and under the action of plasma surface discharge.

Methods

Experimental Methods

Detailed information of the PB-DBD system was provided before, in Ref [22, 23]. The discharge voltage and current are recorded by an oscilloscope (Tektronix MSO44). The discharge power is calculated by the Lissajous method [22]. SF_6 is detected by a gas chromatograph (GC) (Kejie GC8900). Ar, SF_6 and O_2 are mixed by a gas compounder and H_2O is obtained by the evaporation of pure water through a humidity generator. Since the hydration process is closely related to the effective contact area of the packing, we compared two sizes of γ-Al_2O_3 beads (with diameters of 2 and 4 mm). The γ-Al_2O_3 beads have been characterized by BET and SEM, which can be referred in our previous study [23]. For the hydration treatment, the beads are first placed in a humid environment to adsorb water, and the water content is adjusted according to the weight and the adsorption property of the γ-Al_2O_3 beads. They are exposed to the atmospheric environment for one day to reach the state of saturated water absorption. After that, they are packed into the reactor for the DBD plasma experiments. Before each degradation test, a 30-min pre-discharge (Ar charge) is done to ensure that the discharge of the packing system tends to be stable. And the 1-h temporal evolution of the voltage and current signals are shown in Fig. S1 and Fig. S2.

The degradation removal efficiency (DRE) and energy yield (EY) are the two most important key performance indicators. They are used to evaluate the degradation efficacy and they are calculated by measuring the SF_6 concentration before and after plasma abatement.

The DRE is calculated by Eq. 2:

$$\mathrm{DRE} = \frac{C_\mathrm{i} - C_\mathrm{f}}{C_\mathrm{i}} \times 100\% \tag{2}$$

where C_i and C_f are the initial and final concentrations of SF_6, respectively.

The EY is calculated by Eq. 3:

$$\mathrm{EY}(g/\mathrm{kWh}) = \frac{M_{\mathrm{SF}_6}(\mathrm{g}) \times 10^3 \times 3.6 \times 10^3}{P(\mathrm{W}) \times t(\mathrm{s})} \tag{3}$$

where M_{SF_6} is the mass of degraded SF_6 gas, P is the input power, t is the degradation time, and 10^3 and 3.6×10^3 are conversion factors from W to kW, and from s to h.

Computational Details

We performed the DFT calculations by the CP2K 7.0 package [35]. The Quickstep module is chosen for the calculation, employing the Gaussian and plane wave method (GPW) [36, 37]. The Goedecker–Teter–Hutter (GTH) pseudopotentials as well as the polarized double-ζ (m-DZVP) basis sets are selected to describe the core-valence interactions and the expansion of the Kohn–Sham valence orbitals [38]. The cutoff value of the plane wave basis set is chosen at 600 Ry. The exchange correlation functional is described by using the GGA-PBE (Perdew-Burke-Ernzerhof) method [39], with a dispersion correction by Grimme's D3 method [40]. Besides, the K-point sampling is limited to Γ point only, by considering a sufficient supercell size of more than 10 Å in XY directions. The Broyden-Fletcher-Goldfarb-Shanno (BFGS) method is applied for the geometry optimization and the climbing image nudged elastic band (CI-NEB) method is used for the transition state (TS) search calculations [41, 42]. During the calculation, the analysis of the charge transfer process is carried out employing the Bader charge partitioning scheme [43].

The (110) surface is a typical active and stable surface of γ-Al_2O_3, and the lewis acidic sites present on this surface are considered to be the main site for catalytic and activation reactions, which have been widely adopted for use in various thermal and plasma catalysis studies such as CO_2 conversion [33, 44]. The remaining crystalline surfaces may also have catalytic effects, but for computational convenience and representativeness, we chose the γ-Al_2O_3(110) surface structure as the typical model for γ-Al_2O_3 packing. This model is built by a 2×2 supercell containing 160 atoms and is consist of four layers with the XYZ dimensions of $16.14 \times 16.79 \times 40.00$ Å^3. The bottom two layers are fixed during the calculation. The hydrated surface structure of γ-Al_2O_3 is based on the study of Wischert et al.[45].

The setting of the induced charges on the γ-Al_2O_3(110) surface refers to the method proposed by Bal et al. [33]. This method is based on positioning a point charge of $+1.0|e|$ with no basis set assigned, above the slab surface to maintain the surface charging. The electrostatics are described by the Martyna-Tuckerman Poisson solver [46] and the periodicity is limited to XY direction to avoid the non-physical interaction of the slab with itself.

The setting of the external electric field refers to the "dipole sheet" method proposed by Jafarzadeh et al. [47], which is shown schematically in Fig. 1. By setting up two parallel plates of charged atoms at the top and bottom of the surface structure. The atoms in the upper and lower layers of the dipole sheet are positively and negatively charged to form an electrostatic field, and its strength can be adjusted by changing the charge on the plates.

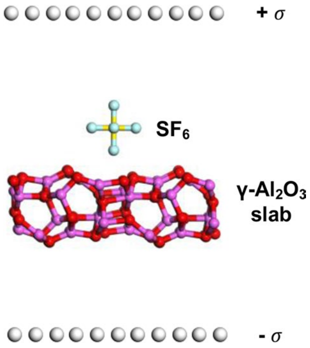

Fig. 1 Dipole sheet method for setting an external electric field

Since the actual reaction process is very short, and occurs at picosecond level, the voltage of one filamentary discharge in DBD is relatively stable during one reaction, and a fixed electric field can be applied when simulate the surface adsorption process [47].

Applying the dipole sheet approach, the strength of the electric field can be expressed in Eq. 4:

$$E = \frac{\sigma}{\varepsilon_0} \tag{4}$$

where E is the electric field with a unit of V/Å, σ is the surface charge density of the dipole sheet, and ε_0 is the vacuum permittivity. In this method, the distance between the two charged plates and the thickness of the plate do not affect the electric field strength. To avoid the interaction with the dummy ions in the plates, the distance between the upper and lower plates is set to 40 Å and the height of the supercell in the Z direction is set to twice the plate spacing, which is 80 Å.

The adsorption energy E_{ad} for the gas molecules on the material surface can be calculated by Eq. 5:

$$E_{\mathrm{ad}} = E_{\mathrm{gas+slab}} - E_{\mathrm{gas}} - E_{\mathrm{slab}} \tag{5}$$

where E_{gas} and E_{slab} are the energy of gas phase molecules and of the slab, respectively, and $E_{\mathrm{gas+slab}}$ is the total energy of the system after the adsorption. When E_{ad} is negative, it indicates that the energy of the system is reduced due to adsorption. A more negative value of E_{ad} is indicative of a more stable adsorption mode, corresponding to a stronger interaction between the adsorbed species and the surface.

Results and Discussion

Hydration Effect on SF_6 Degradation

Discharge Parameters

We first study the effect of moisture exposure. As shown in Fig. 2, the hydration process shows reduction effects on the discharge voltage for both the 2 and 4 mm packing systems. In the 2 mm system, the voltage of hydrated beads packing is always lower than that in the dry system. By contrast, in the 4 mm system, the voltage of the hydrated system becomes close to the dry system when the input power arrives 80 W. This result indicates that the effect of moisture on the discharge process of the γ-Al_2O_3 packing varies with the bead size. Besides, the filamentary character is reduced in the hydrated systems, especially in the 2 mm packing system, as shown in Fig. S3, which could be attributed to the change of surface properties of the γ-Al_2O_3 packing by the hydration treatment.

The Q–V plots for the 2 and 4 mm packing systems before and after the hydration are shown in Fig. S4. The slope of line AB and CD decreases in both systems, corresponding to a decrease of the equivalent dielectric capacitance (ζ_{diel}) in the discharge-on phase [48, 49]. This indicates that the discharge in the hydrated system is less stable. It should be noted that the relative permittivity of H_2O (78.5) is obviously greater than that of γ-Al_2O_3 (10.0), and the equivalent dielectric capacitance of the packing should be increased after the hydration. However, the decrease of ζ_{diel} indicates that the discharge is inhibited by moisture adsorption [49, 50]. This may be caused by two main reasons. Firstly, the

Fig. 2 Effects of hydration on the discharge voltage against input power, for the 2 mm and 4 mm γ-Al_2O_3 packing systems (3% SF_6–97% Ar, 100 mL/min)

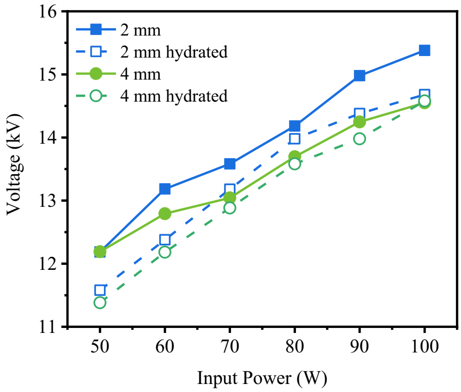

adsorbed H_2O on the packing surface could reduce the filamentary discharge character, thus inhibiting the maintenance of the plasma. On the other hand, H_2O could ionize or evaporate during the discharge, thus consuming energy.

DRE and EY

We present the DRE and EY results in Fig. 3. In Fig. 3a, the DRE is significantly reduced by the hydration treatment and the 2 mm packing system is more seriously affected than the 4 mm packing. In the 2 mm packing system, the DRE is ca. 40% at 50 W and gradually increases to ca. 50% at 100 W, much lower than in the dry system (where it varies between 65 and 100%). In the 4 mm packing system, the DRE increases from ca. 58% at 50 W to ca. 68% at 100 W. In contrast, the DRE in the 2 and 4 mm dry packing systems exceeds 99% and 90%, respectively, when the input power exceeds 80W. The above results indicate that the hydration process significantly inhibits the SF_6 degradation, and makes the DRE rather insensitive to the input power. In Fig. 3b, the hydrated packing also significantly reduces the EY. In the 2 mm hydrated packing system, the EY drops from 9.46 g/kWh at 50 W to 5.82 g/kWh at 100 W. In the 4 mm

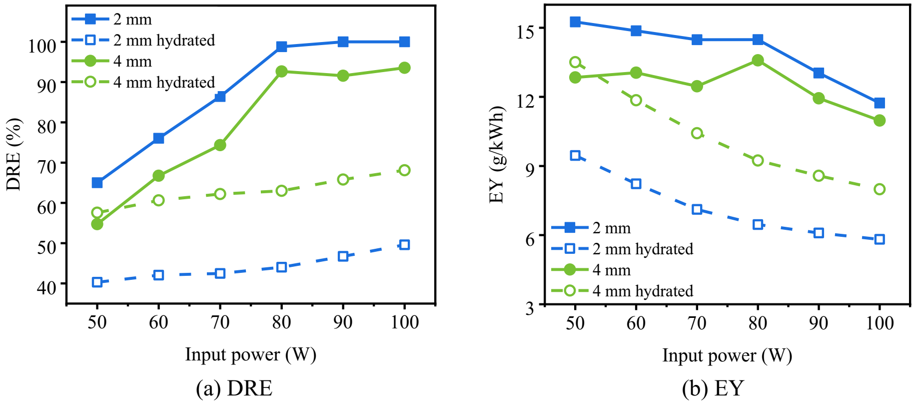

(a) DRE (b) EY

Fig. 3 DRE and EY as a function of input power in two γ-Al_2O_3 packing systems, before and after hydration (3% SF_6–97% Ar, 100 mL/min) hydrated packing system, the EY drops from 13.51 g/kWh at 50 W to 7.99 g/kWh at 100 W. In our previous study, the EY could reach about 5 g/kWh in a non-packed system at 150 mL/min and 2% SF_6 initial concentration [22]. Therefore, the inhibition caused by the hydration almost compensates for the promotion effect of the packing system on the SF_6 abatement.

Compared with the change in the discharge signals and the discharge power, the DRE is more seriously reduced by the hydration. This suggests that, rather than a change in discharge parameters, a change in surface state of the packing beads will be responsible for the dramatic inhibition of the SF_6 degradation. Moreover, since the 2 mm packing has a larger effective contact area than the 4 mm packing, it is more severely reduced by the hydration process, which also suggests that the surface structure of the beads is a key factor for the effect on the DRE. As discussed in the Introduction, the hydration process leads to the adsorption of H_2O molecules on the γ-Al_2O_3 surface, which can hinder the adsorption and activation of SF_6 on the packing surface. We will discuss this in more detail when analyzing the DFT results in Sect. "Initial bond-breaking process" below.

Fig. S5 shows the FTIR results of the degradation products in the hydrated γ-Al_2O_3 packed bed DBD system. Except for the remaining SF_6, the other gases involve SF_4, S_2F_{10}, SOF_2, SO_2F_2 and SOF_4, which shows a typical product distribution of the DBD treatment [15]. However, there is no signal of SO_2, which indicates that the degradation is not sufficient to fully dissociate SF_6 into S and F atoms. We hypothesize that pre-adsorption of H_2O on the γ-Al_2O_3 surface reduces the decomposition of SF_6 molecules, thus prohibiting the further decomposition of the intermediates. The reaction mechanism will be further analyzed by our DFT calculations in Sect. "Initial bond-breaking process" below. Moreover, SOF_4 and SO_2F_2 in the tail gas are two gases relatively difficult to be treated [51]. This means that the hydration of the packing not only negatively impacts the degradation performance, but also has a negative effect on the product distribution.

In summary, the surface state should be carefully evaluated when choosing γ-Al_2O_3 as the packing material in industrial applications. First of all, the γ-Al_2O_3 packing should be kept dry for the first packing. Second, in the case of long-term operation, the packing in the reactor should be heated and dehydrated before a degradation treatment. If the reactor is not resistant to high temperature, dry air or other gases (Ar, N_2 etc.) should be introduced to pre-treat the packing, so that the possible adsorbed H_2O can be removed, to prevent it from affecting the SF_6 degradation.

H_2O and O_2 Addition on SF_6 Degradation

In this section, we focus on the effect of the presence of H_2O and O_2 on the degradation process. Previous studies have demonstrated that a proper amount of reactive gas contributes to the SF_6 degradation, while an excessive addition has negative effects [52]. Both the discharge parameters and the degradation efficiency are considered here. Subsequently, the optimal gas concentrations of H_2O and O_2 for this packed bed system and the trend of the DRE variation are determined.

Discharge Parameters

Fig. S6 shows the discharge voltage and current of the systems with H_2O and O_2 added, for the DRE-optimal (a,b) and maximum (c,d) added concentrations. Compared to the dry

4 mm packing without reactive gases in Fig. S3(d), the amplitudes of voltage and current in Fig. S6 are a bit smaller, because the input power is lower than in Fig. S3. However, the filamentary character in the current signals of both systems after adding H_2O or O_2 is slightly more apparent, indicating that the micro-discharges are slightly enhanced, which promotes the generation of reactive species, thus facilitating the SF_6 degradation. By comparison within Fig. S6, we can see that the concentration of the reactive gases shows limited effects on neither the amplitudes nor the filaments. Furthermore, the Q–V plots for the discharge systems with and without additional gases, shown in Fig. S7, are quite similar for all three conditions. These results show that the reactive gases hardly affect the discharge parameters, which is probably due to their low concentrations.

DRE and EY

In Fig. 5, we plot the DRE and EY as a function of added H_2O and O_2 concentration, for an input power of 80 W. Since we observed before [52] that H_2O and O_2 can promote the SF_6 degradation in plasma without packing, we increased the flow rate to 200 mL/min to test their promotion potentials. From Fig. 4 we can see that with increase of the additional gases, the DRE and EY first increase and eventually decrease. In Fig. 4a, 0.5% is the optimal concentration for H_2O addition, reaching a DRE of 93% and an EY of 24.94 g/kWh. When the H_2O concentration exceeds 0.5%, the DRE and EY gradually decrease and finally reach 65% and 17.70 g/kWh at 2.5% H_2O. Similarly, the DRE and EY first increase to a maximum of 81% and 21.63 g/kWh, respectively, at 0.1% O_2, but with increasing O_2 concentration, they eventually drop to 43% and 11.63 g/kWh at 4% O_2.

Generally, these two gases both show a promotion effect at low concentrations, and H_2O is a bit better than O_2. In Ref [52], the optimal ratio of O_2:SF_6 is 1:1 in the non-packed system which is much higher than that in the γ-Al_2O_3 packed system (1:30, Fig. 4b). Meanwhile, our previous study found that the variation of γ-Al_2O_3 bead size slightly affects the discharge behavior, but significantly changes the degradation performance. Lowing the bead size increases the contact area, resulting in a higher DRE and SO_2 yields, which corresponds to a more efficient SF_6 degradation and S-F detachment. This indicates that the γ-Al_2O_3 surface could be the main reaction area. In this experiment, the DRE starts to decrease significantly when the (reactive gas:SF_6) ratio was much less than 1:1 for either H_2O or O_2, while their discharge parameters did not change significantly compared to the

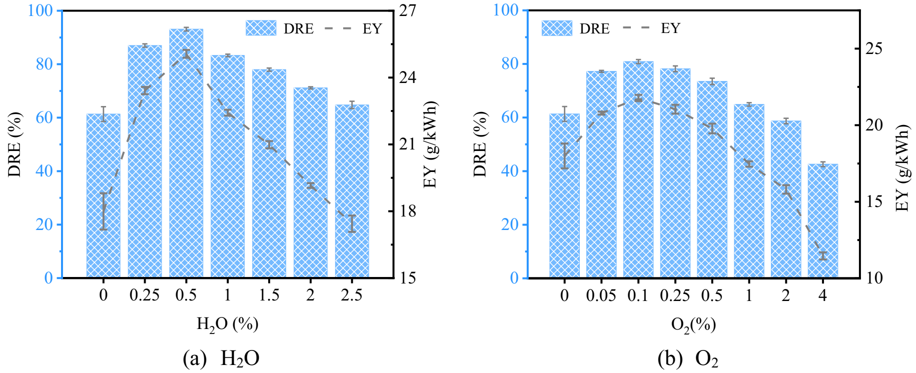

(a) H_2O (b) O_2

Fig. 4 DRE and EY upon H_2O or O_2 addition (80 W, 200 mL/min, 3% SF_6, 4 mm γ-Al_2O_3 packing) dry bead system (Fig. S6). On the other hand, the most extreme condition of excessive H_2O addition should be similar to the hydration system, i.e., the γ-Al_2O_3 surface has excessive or saturated moisture accumulation. The results from Figs. 2 and 3 show that the decrease in DRE due to hydration is more significant than the suppression of discharge. Therefore, we may speculate that the excess reactive gas inhibited the degradation effect mainly by affecting the gas–solid interface reactions. This will be further investigated by our DFT calculations in the following sections.

SF_6 Adsorption and Decomposition on Different Types of γ-Al_2O_3 (110) Surfaces: Effects of Hydration and Addition of Reactive Gases, Revealed by DFT Calculations

Adsorption

According to our previous study, the Al_{III} is selected as the active site for adsorption [23]. We consider three surface conditions (hydrated, H_2O and O_2), as they correspond to the experimental conditions when the surface of the packing material is hydrated, or when additional gases (H_2O and O_2) are added [52–54]. Here we present the calculated configurations of SF_6 molecules adsorbed on these three types of surfaces (Fig. S8 and Fig. S9), as well as the E_{ad} values (Table 1).

As shown in Table 1, on the hydrated γ-Al_2O_3 surface, E_{ad} is -0.39 eV. Its absolute value is slightly smaller than that on the perfect surface (-0.41 eV). Meanwhile, Fig. S8(a) shows that there is no obvious bonding process after the adsorption, which indicates that the SF_6 adsorption is weakened on the hydrated surface, as the Al_{III} sites are occupied by OH and H. Besides, on the H_2O pre-adsorbed surface, the system has a larger adsorption energy when H_2O is pre-adsorbed at the Al_{III} site, with a total E_{ad} reaching -1.72 eV. If SF_6 is adsorbed at the Al_{IV} site, the total E_{ad} is only -1.59 eV. However, on the O_2 pre-adsorbed surface, the system with SF_6 adsorbed at the Al_{III} site has a larger E_{ad} of -1.03 eV. The above results indicate that H_2O molecules are more likely to occupy the Al_{III} site rather than O_2 and it could form a stable adsorption structure when the γ-Al_2O_3 packing surface is subjected to moisture. In contrast, the effect of O_2 addition is relatively weak and the overall E_{ad} on the γ-Al_2O_3 surface is much lower.

In summary, the pre-adsorbed species, i.e., H, OH, H_2O and O_2, occupy the active sites and weaken the SF_6 adsorption process, which could be the main reason for the reduction

Table 1 E_{ad} of SF_6 molecules on different γ-Al_2O_3 surfaces

Surface type	Site for pre-adsorbed molecules	Site for SF_6	E_{ad} (eV)
Perfect γ-Al_2O_3	–	Al_{III}site	– 0.41[23]
Hydrated γ-Al_2O_3	–	Unbonded	– 0.39
H_2O pre-adsorbed	Al_{II}	Unbonded	– 1.72[a]
	Al_{IV}	Al_{III}site	– 1.59[a]
O_2 pre-adsorbed	Al_{I}	Unbonded	– 0.88[b]
	Al_{IV}	Al_{III}site	– 1.03[b]

[a] E_{ad} is the total adsorption energy of H_2O and SF_6

[b] E_{ad} is the total adsorption energy of O_2 and SF_6

of SF_6 degradation when the γ-Al_2O_3 is hydrated or excessive reactive gases are added. Meanwhile, in Fig. S9, the adsorption of SF_6 molecules at the Al_{III} site does not have a bonding process, even if H_2O or O_2 does not occupy this site. This indicates that the adsorbed species near the active site may also have some slight reduction effects on SF_6 adsorption. It should be noted that the high-energy H and OH species that may participate in the reaction could be generated from the dissociation of H_2O in the plasma [55]. Besides, the H_2O molecule approaches the γ-Al_2O_3 surface could occur a decomposition to form adsorbed H* and OH* species (* means the adsorption state) [45]. Overall, the occupation of the active sites could play an important role in the reduction of the degradation performance caused by either the excess reactive gases or by the hydration of the packing beads.

Initial Bond-Breaking Process

We calculated the initial bond-breaking processes of SF_6 on the three γ-Al_2O_3 surfaces. The activation barrier E_a and the reaction heat ΔE are presented in Table 2. The reaction occurs in Eq. 6:

$$SF_6 \rightarrow SF_5 + F \tag{6}$$

The direct S-F bond breaking in the gas phase needs an E_a of 4.20 eV, which is much higher than on each γ-Al_2O_3 surface. If the surface is hydrated or has O_2 pre-adsorbed (at an Al_{IV} site), the E_a increases to 1.92 and 1.97 eV, respectively. Besides, if a H_2O molecule is pre-adsorbed at an Al_{IV} site (near the Al_{III} site), the E_a decreases to 1.50 eV. The reaction heats are different at the four different surfaces. The reaction is endothermic only on the hydrated surface and exothermic on the other three surfaces.

To further investigate the possible facilitating role of H_2O pre-adsorption, the TS process of this reaction on H_2O pre-adsorbed surface is shown in Fig. 5, and the TS processes of SF_6 initial bond breaking on the O_2 pre-adsorbed and hydrated surfaces are shown in Fig. S10.

In Fig. 5, the lateral S-F bond breaks and the F-5 atom (see label in left panel) creates a bond with two surface Al atoms, while the SF_5 remains attached to the Al_{III} atom. In this process, the H_2O remains stable without obvious structure deformation. However, on the perfect γ-Al_2O_3 surface, the bottom S-F bond breaks first and the SF_5 radical displaces and creates a bond with the surface O atom, while the bottom F remains attached to the Al_{III} atom [23]. Therefore, the TS process over a H_2O pre-adsorbed surface is different from that on the perfect γ-Al_2O_3 surface, which indicates a change of the bond-breaking process of the adsorbed SF_6 caused by the pre-adsorbed H_2O.

Table 2 Activation barrier E_a and reaction ΔE heat in different conditions

Condition	E_a (eV)	ΔE (eV)
Gas phase	4.20 [23]	–
Perfect γ-Al_2O_3	1.80 [23]	– 1.29
Hydrated γ-Al_2O_3	1.92	0.69
H_2O pre-adsorbed[a]	1.50	– 1.35
O_2 pre-adsorbed[a]	1.97	– 0.69

[a] H_2O or O_2 adsorbed at sites near the Al_{III} site

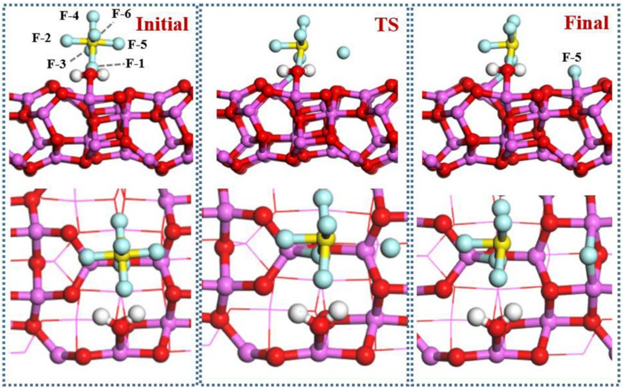

Fig. 5 TS process of SF_6 initial bond breaking on H_2O pre-adsorbed surface

The Bader charge of SF_6 before and after the initial S-F bond breaking in both the perfect and H_2O pre-adsorbed conditions are shown in Table 3. On the H_2O pre-adsorbed surface, the S atom gains 2.47|e| electrons, and its valence state changes after the bond breaking. By contrast, the electron distribution of the S atom remains unchanged on the perfect surface and the change in the partial charge of the F atoms on the perfect surface is smaller than on the H_2O pre-adsorbed surface. In the gas phase, the leaving F-5 atom loses 0.74|e| and the S atom gains 0.79|e|. This suggests that on the H_2O pre-adsorbed surface, a charge transfer process from the γ-Al_2O_3 slab to SF_6 occurs during the S-F bond-breaking, resulting in a lower valence state of the S atom.

Fig. S11 shows the differential charge distribution of SF_6 on the H_2O pre-adsorbed surface before the bond breaking, where the yellow and cyan regions indicate an increase and decrease in charge density, respectively. In Fig. S11, the H_2O pre-adsorption affects the surface charge transfer process. At the surface Al_{III} site, yellow regions near the Al and S

Table 3 Bader charge distribution of SF_6 before and after the initial S-F bond breaking in the gas phase, on perfect and H_2O pre-adsorbed surfaces

Atom	Gas phase			Perfect γ-Al_2O_3			H_2O pre-adsorbed γ-Al_2O_3		
	Before	After	Charge difference	Before	After	Charge difference	Before	After	Charge difference
S	0	0.79	0.79	0.00	0.00	0.00	0.00	2.47	2.47
F-1	8.01	7.98	– 0.03	8.01	7.97	– 0.03	8.01	7.93	– 0.08
F-2	7.99	8.04	0.05	8.02	7.97	– 0.05	8.02	8.02	– 0.00
F-3	7.99	7.98	– 0.01	8.01	8.01	0.00	8.00	7.59	– 0.41
F-4	8.01	7.97	– 0.04	8.01	8.01	0.00	8.01	8.08	0.07
F-5	8.00	7.26	– 0.74	7.99	8.02	0.03	8.00	8.02	0.02
F-6	8.00	7.98	– 0.02	8.00	8.00	– 0.00	8.00	7.90	– 0.10
Sum	0	0	0	0.04[a]	– 0.02[a]	– 0.05	0.04[a]	2.01[a]	1.97

[a] The total charge here is the value after deducting the number of electrons in the valence layer of each atom of S and F (6 for S and 7 for F), which shows the overall charge change of the SF_6 molecule itself after the chemical reaction. Positive values indicate the gain of electrons. F atoms are labeled in Fig. 5

atoms indicate their gain of electrons, while the cyan region near the bottom F indicates the loss of electrons. The electron transfer process could be the main reason for stretching of the S-F bond and the activation of SF_6, promoting its degradation. Meanwhile, the overall color of H_2O is cyan, which indicates the loss of electrons. This phenomenon indicates that some electrons may be transferred from H_2O to the γ-Al_2O_3 surface after the pre-adsorption, changing the electron distribution on the surface, and eventually resulting in the promotion of the SF_6 bond breaking. This could be a reason for the better promotion effect of H_2O than O_2 in Fig. 5.

Plasma-Induced Surface Effects, as Revealed by DFT Calculations

Effect of Excess Electrons

By adding one + 1.00 |e| charged proton above the slab surface, the γ-Al_2O_3 surface is negatively charged with 1.00 |e|. The adsorption energy E_{ad} and the length variation of the bottom S-F bond over three surfaces are listed in Table 4 and the configurations are shown in Fig. 6. In Fig. 6a, on the perfect γ-Al_2O_3 surface, the E_{ad} increased from – 0.41 eV without excess electrons to -3.55 eV, corresponding to a chemical adsorption, along with the bottom S-F bond length stretching from 1.61 to 2.11 Å [23]. On the H_2O and O_2 pre-adsorbed surfaces, the E_{ad} increased from – 1.59 and – 1.03 eV to – 5.36 and – 3.93 eV, with the S-F bond stretching from 1.61 to 2.29 Å and 2.10 Å, respectively. Compared with the three systems, SF_6 has the strongest adsorption process on the H_2O pre-adsorbed surface and the stretching of the bottom S-F bond is close to a bond breaking process. In other words, the plasma-induced surface charge may enhance the SF_6 adsorption and elongate the S-F bonds, which promotes the activation of SF_6 molecules on the packing surface.

To further study the effect of plasma-induced surface charges on the SF_6 adsorption process, we carried out the Bader charge analysis, as shown in Table 5. Compared to the electrically neutral system in Table 3, the surface induced electrons significantly change the charge distribution of SF_6, especially the S atom. The S atoms obtained 1.89 |e|, 2.15 |e| and 1.66 |e| on the perfect surface, the H_2O pre-adsorbed surface and the O_2 pre-adsorbed surface, respectively. Besides, SF_6 gains more charges than in the electrically neutral system. Within the SF_6 molecule, the S atom gained electrons while the F atoms mainly lost electrons, which is supported by the differential charge distribution results in Fig. S12. Comparing Fig. S12 (a) and (b), both systems show significant charge transfers between the bottom F atom and the Al_{III} site, the H_2O pre-adsorbed system is stronger. This charge transfer process leads to a change in the valence state of S and F atoms, which could enhance the chemical adsorption and the activation of SF_6 molecules over the packing surface.

Table 4 Adsorption energy E_{ad} and bottom S-F bond length variation at the Al_{III} site on three surfaces

Surface type	E_{ad} (eV)	Bottom S-F bond length (Å)
Perfect γ-Al_2O_3	– 3.55	2.11
H_2O pre-adsorbed γ-Al_2O_3	– 5.36[a]	2.29
O_2 pre-adsorbed γ-Al_2O_3	– 3.93[a]	2.10

[a] E_{ad} is the total adsorption energy of SF_6 and the pre-adsorbed species

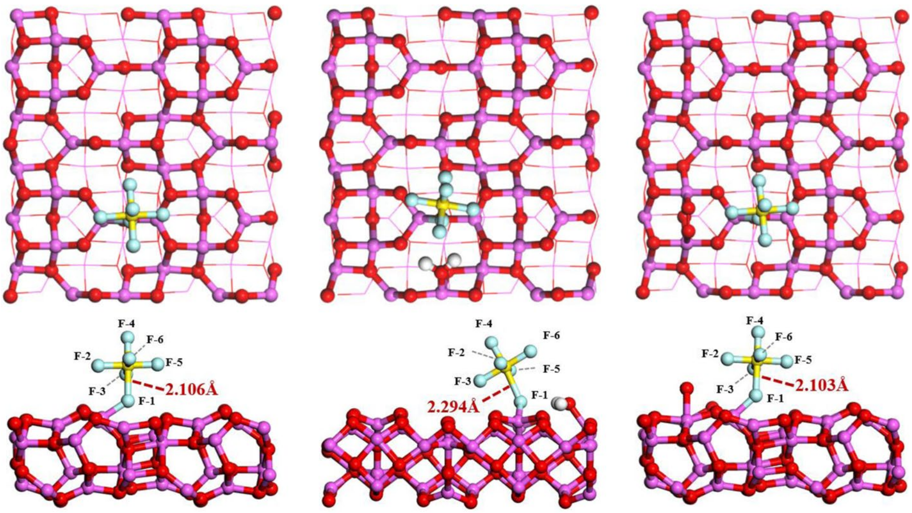

(a) Perfect γ-Al_2O_3 (b) H_2O pre-adsorbed γ-Al_2O_3 (c) O_2 pre-adsorbed γ-Al_2O_3

Fig. 6 SF_6 adsorption configurations on three 1.00|e| negatively charged γ-Al_2O_3 surfaces

Table 5 Bader charge analysis of the SF_6 molecule on three 1.00|e| negatively charged surfaces

Atom	Perfect γ-Al_2O_3		H_2O pre-adsorbed γ-Al_2O_3		O_2 pre-adsorbed γ-Al_2O_3	
	Bader charge	Charge variation	Bader charge	Charge variation	Bader charge	Charge variation
S	1.89	1.890	2.15	2.15	1.66	1.66
F-1	7.83	– 0.17	7.90	– 0.10	7.80	– 0.200
F-2	7.59	– 0.41	7.57	– 0.43	7.59	– 0.41
F-3	7.77	– 0.23	8.00	0.00	7.55	– 0.45
F-4	8.11	0.11	8.07	0.07	8.12	0.12
F-5	8.04	0.04	7.88	– 0.12	8.02	0.02
F-6	7.64	– 0.36	7.51	– 0.49	8.09	0.09
Sum	–	0.87[a]	–	1.08[a]	–	0.83[a]

[a] The total charge here is the value after deducting the number of electrons in the valence layer of each atom of S and F (6 for S and 7 for F). F atoms are labeled in Fig. 7

Effect of External Electric Field

We take the perfect γ-Al_2O_3 slab as the example to study the effects of the external field. Two directions of the electric field are considered. The "↓" and "↑" symbols are used to describe the direction of the electric field which is opposite or along the z-axis direction. The adsorption energy and bottom S-F bond length of SF_6 on the perfect γ-Al_2O_3 surface under different electric field strengths are summarized in Table 6 and Fig. 7. The

Table 6 Adsorption energy E_{ad} and bottom S-F bond length variation for SF_6 adsorption on perfect γ-Al_2O_3 surface under different electric fields

E-field strength V/ Å	↓[a] electric field		↑[a] electric field	
	E_{ad} (eV)	Bottom S-F bond length (Å)	E_{ad} (eV)	Bottom S-F bond length (Å)
0.00	– 0.41	1.70	– 0.41	1.70
0.25	– 0.38	1.67	– 0.62	1.73
0.50	– 0.34	1.65	– 0.84	1.78
0.60	– 0.35	1.70	– 0.89	1.80
0.75	– 0.69	2.08	– 1.08	1.84
0.80	– 0.92	2.14	–	–
0.85	– 1.00	2.15	–	–
0.90	– 1.18	2.18	–	–
1.00	–	–	– 1.41	1.94
1.25	–	–	– 1.84	2.00
1.50	–	–	– 2.40	2.24

[a] The "↓" and "↑" symbols mean that the direction of the external electric field is opposite or along the z-axis direction

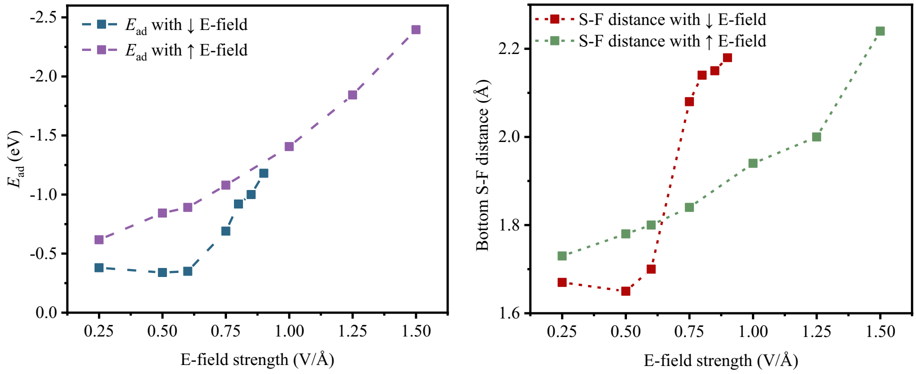

(a) E_{ad}

(b) Bottom S-F distance

Fig. 7 Adsorption energy E_{ad} and bottom S-F bond length as a function of the electric field strength

aggregated surface partial charges of the perfect γ-Al_2O_3 slab under different electric field strengths are shown in Fig. S13.

When the ↓ electric field is applied, the E_{ad} of SF_6 slightly decreases and then increases rapidly with increasing the electric field. When the electric field strength is less than 0.75 V/Å, the E_{ad} as well as the bottom S-F bond length are smaller than on the natural surface, corresponding to a physical adsorption of SF_6 on the γ-Al_2O_3 surface, as shown in Fig. 8a. When the ↓ electric field strength exceeds 0.75 V/Å, the adsorption process changed significantly, and the E_{ad} increases to -0.69 eV with the S-F bond length stretching to 2.08 Å. The state of SF_6 is likely to change from physical adsorption

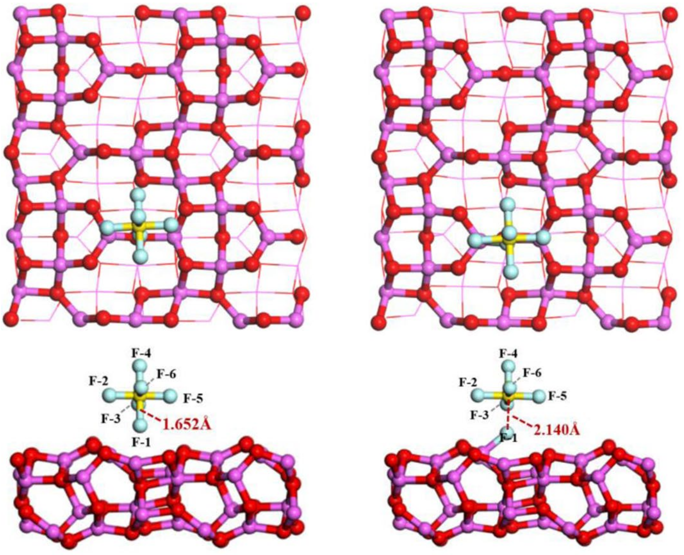

(a) 0.50V/ Å of ↓ electric field (b) 0.80V/ Å of ↓ electric field

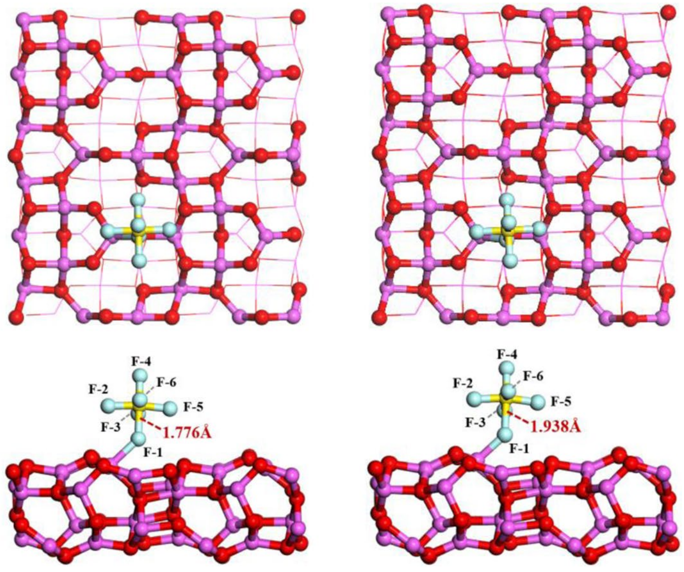

(c) 0.50V/ Å of ↑ electric field (d) 1.00V/ Å of ↑ electric field

Fig. 8 SF_6 adsorption configurations under two electric field strengths (↓ and ↑ means the direction of the electric field opposite or along the z-axis direction, respectively)

to chemical adsorption. At 0.80 V/Å, the E_{ad} increased to -0.92 eV and the S-F bond length increased to 2.14 Å. In Fig. 8b, SF_6 undergoes a significant chemical adsorption.

Bader analysis of the SF_6 adsorption configurations under different electric fields are shown in Table 7. At the range of 0.50 V/ Å ↓ electric field, SF_6 gains almost no additional charge and the valence state of the S atom remains unchanged. However, when the electric field increases to 0.80 V/ Å ↓, the S atom gains + 1.686 |e| electrons and the SF_6 molecule gains + 0.59 |e|, which is also verified in the differential charge distribution results in Fig. S14. This indicates that increasing the electric field promotes the charge transfer from the slab surface to SF_6, causing significant stretching of the bottom S-F bond. By comparison, applying the ↑ electric field has slightly impacts the Bader charge of the SF_6 molecules, and the number of electrons obtained by S decreases with the ↑ electric field. As shown in Fig. S13, the amount of positive charge on the top slab surface increases with the field strength and it may inhibit the charge transfer from slab to SF_6, especially to the S atom.

The PDOS (Projected density of state) of the above systems are shown in Fig. 9. In Fig. 9b and d, the distributions of the outer valence electron orbitals of the atoms are shifted toward the Fermi level, indicating a stronger overlapping of orbitals between SF_6 and surface atoms, which does not happen in Fig. 9a and only happens in O orbitals in Fig. 9c. This indicates that the increase of the electric field improves the interaction between SF_6 molecules and surface atoms, leading to a stronger charge transfer process and the electron orbital interactions, eventually affecting the surface bonding between SF_6 and the surface atoms. In general, this process eventually leads to the transition of SF_6 adsorption type from physical to chemical, accompanied by the stretching of S-F bonds.

It should be noted that the field strength of 0.25–0.90 V/Å is a large value that far exceeds the average applied field strength in an ordinary DBD system. However, in realistic conditions, phenomena such as charge accumulation and the micro discharge formations could lead to a sudden increase in local electric fields inside a DBD reactor bringing it to the ranges computationally discussed here [24, 56]. Besides, the DFT simulations used here are aimed at understanding the atomic and molecular interactions via an isolated and computationally approximated approach, to give a qualitative explanation for the electric field effect, similar to the studies that have shown methodological feasibility [47, 57].

Table 7 Bader charge analysis of SF_6 adsorption configurations under different electric field strengths

Atom	↓ electric field				↑ electric field			
	0.50 V/ Å		0.80 V/ Å		0.50 V/ Å		1.00 V/ Å	
	Bader charge	Charge variation	Bader charge	Charge variation	Bader charge	Charge variation	Bader charge	Charge variation
S	0.00	0.00	1.69	1.69	0.24	0.24	0.15	0.15
F-1	8.03	0.03	7.81	– 0.19	7.72	– 0.28	7.71	– 0.29
F-2	8.02	0.02	7.76	– 0.24	8.02	0.02	7.98	– 0.02
F-3	8.01	0.01	8.15	0.15	8.02	0.02	8.09	0.09
F-4	8.02	0.02	8.04	0.04	8.03	0.03	8.04	0.04
F-5	7.97	– 0.03	7.67	– 0.33	7.99	– 0.02	8.00	0.00
F-6	7.99	– 0.01	7.48	– 0.52	8.05	0.05	8.08	0.08
Sum	–	0.04	–	0.59	–	0.06	–	0.05

[a] The total charge here is the value after deducting the number of electrons in the valence layer of each atom of S and F (6 for S and 7 for F). F atoms are labeled in Fig. 8

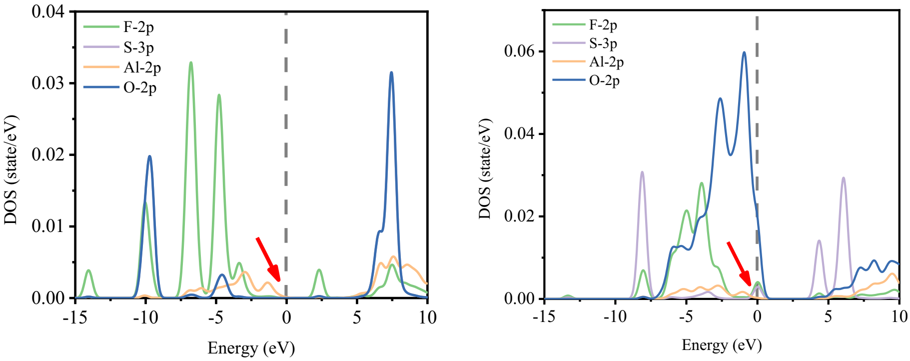

(a) 0.50V/ Å of ↓ electric field (b) 0.80V/ Å of ↓ electric field

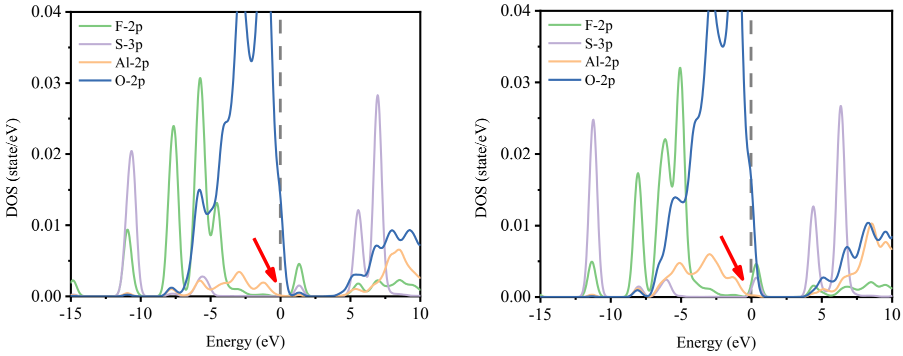

(c) 0.50V/ Å of ↑ electric field (d) 1.00V/ Å of ↑ electric field

Fig. 9 PDOS of SF_6 adsorption configurations under different electric field strengths

Synergistic Effect of Excess Electrons and External Electric Field

Here we use the dipole sheet method to investigate the combined effects of excess electrons and external electric field on the SF_6 adsorption. The surface induced charge is kept at -1.00|e| and the ↓ electric field strength is varied from 0.10 to 0.50 V/ Å. The adsorption results are shown in Table 8 and Fig. 10.

Table 8 Adsorption energy E_{ad} and bottom S-F bond length variation for SF_6 adsorption under the condition of 1.00|e| charge and different ↓ electric field strengths

E-field strength V/ Å	E_{ad} (eV)	Bottom S-F bond length (Å)
0.10	– 3.35	2.09
0.20	– 3.51	2.15
0.30	– 3.66	2.17
0.40	– 3.78	2.17
0.50	– 4.00	2.17

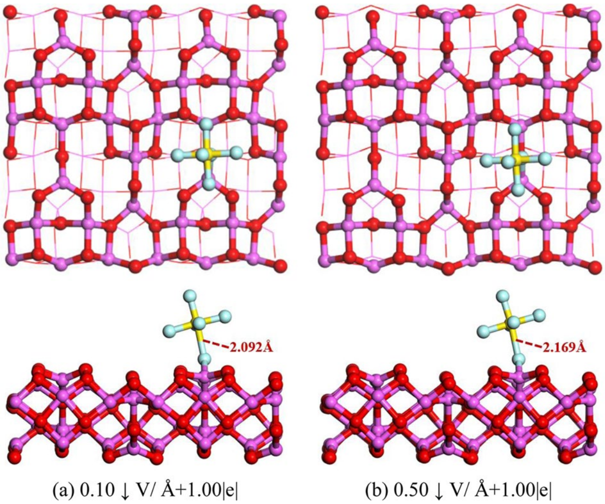

(a) 0.10 ↓ V/ Å+1.00|e| (b) 0.50 ↓ V/ Å+1.00|e|

Fig. 10 SF_6 adsorption configurations with excess electrons and external electric field

Compared with the 'electron only' results in Table 4, applying a 0.10 V/ Å electric field slightly reduces the E_{ad} of SF_6 and the elongation of the bottom S-F bond. The SF_6 configuration at 0.10 V/Å + 1.00|e| condition in Fig. 10a is similar to "no electric field" condition shown in Fig. 6a. This indicates the electric field at this level has only a marginal effect on the adsorption system. However, when the field strength continued to increase, the adsorption process of SF_6 is enhanced. At 0.50 ↓ V/ Å + 1.00|e|, the E_{ad} increases to -4.00 eV while the S-F bond length stays constant at 2.17 Å, as shown in Fig. 10b. At this stage, the SF_6 molecule is fully activated and is prone to a further decomposition. In Sect. "Effect of external electric field", when 0.50 V/ Å electric field is applied without excess electrons, the E_{ad} is only -0.34 eV, much less than the -4.00 eV in this system. Therefore, the excess electrons and external electric field have an obvious synergistic effect and can jointly promote the adsorption and activation of SF_6 over the packing surface.

In summary, the regulation of the plasma-induced surface effects could be an effective way to enhance the SF_6 degradation rate as well as the product selectivity. In practice, the reaction conditions for the gas–solid interface can often be conditioned by three aspects: catalyst, discharge and reactive gases.

(1) The change of catalyst structure is of great importance in regulating surface reactions, such as forming a porous structure and increasing the micro-discharge [58]. Another method is to load metals over the support catalyst (γ-Al_2O_3), thus affecting the surface reactions by metal active sites and the metal-support interaction [59]. In addition, this study indicates that the over-adsorption on the catalyst surface needs to be prevented, which affects the interaction of the active sites with the SF_6 (target) molecules.
(2) For NTP discharge, increasing the reduced electrical field strength (E/N) in a certain range is a practical method, which facilitates the active particle density and enhancing the adsorption as well as the activation process of gas molecules over the catalyst surface [17].
(3) In NTP treatment, the addition of proper reactive gases such as O_2, H_2O, H_2, etc. should also be considered. Active particles are generating in the plasma region and affect the

surface reactions via Langmuir– Hinshelwood and Eley–Rideal mechanisms [59], thus hindering the SF_6 self-recovery process and enhancing the S-F separation.

Therefore, multiple methods could be considered for the SF_6 degradation enhancement in the future. At the same time, advanced experenmtal methods like in-situ diacharge diagnosis and surface characterizations, and multi-scale physi-chemical simulations should be applied to gain more detailed insights for the SF_6 decomposition mechamisn in a complex plasma system.

Conclusions

In this study, we performed both experiments and DFT calculations to investigate the effects of hydration and of reactive gas addition as well as the plasma-induced surface effects on SF_6 degradation in a packed bed DBD plasma. Our experiments reveal that the degradation process is significantly reduced when the packing is hydrated by exposure to moisture, especially for small size packing. However, the hydration process hardly changes the discharge behavior and only slightly decreases the effective dielectric capacitance. In addition, in a 4 mm γ-Al_2O_3 packing system, the optimal concentrations of H_2O and O_2 are 0.5% and 0.1%, respectively. Higher addition of H_2O or O_2 reduces both the DRE and EY, while it barely affects discharge parameters.

Our DFT calculations reveal that the occupation of the active sites (Al_{III} site) on γ-Al_2O_3 by adsorbed species such as OH, H_2O, and O_2 can reduce the SF_6 adsorption and prevent its surface binding process. This corresponds well with the poor SF_6 degradation results in our experiments. Besides, the H_2O pre-adsorbed near the Al_{III} site can promote the initial decomposition of SF_6 and this may be due to the change of the electronic structure of the γ-Al_2O_3 surface by the H_2O adsorption, leading to an enhancement of the activation process of SF_6 molecules. Plasma-induced surface charges and external electric field caused by the plasma on the γ-Al_2O_3 surface can improve the adsorption and the activation of SF_6. We found that 1.00 |e| negatively charged surface shows a chemisorption of SF_6. 0.75 V/Å is the turning point of SF_6 adsorption behavior in '↓' direction electric field, and the adsorption energy as well as the bottom S-F bond length dramatically increase when exceeding this electric field strength. However, this phenomenon does not happen in the ↑ direction electric field. Moreover, we found that the synergistic effect of the plasma-induced surface charges and local electric field on SF_6 decomposition. 0.50 V/Å (↓ direction) + 1.00|e| condition could lead to a stable chemisorption of SF_6 over the perfect γ-Al_2O_3 surface.

In summary, our study indicates that the surface structure of the γ-Al_2O_3 packing and the plasma effects are crucial for the catalytic degradation of SF_6. Hence, the input gas conditions as well as the packing surface structure should be carefully evaluated when using γ-Al_2O_3 as the packing material or the catalyst support in SF_6 DBD treatment. It is important to keep the packing surface dry with sufficient active sites during the SF_6 degradation. Moreover, our DFT results indicate that the plasma-induced surface charges significantly impact the packing surface properties as well as the surface reactions. Therefore, regulating the plasma-induced surface effects could be an effective way to enhance the SF_6 degradation rate as well as the product selectivity.

Supplementary Information The online version contains supplementary material available at https://doi.org/10.1007/s11090-023-10320-3.

Acknowledgements The computational resources and services used in this work were provided by the HPC core facility CalcUA of the Universiteit Antwerpen, and VSC (Flemish Supercomputer Center), funded by the Research Foundation—Flanders (FWO) and the Flemish Government.

References

1. Christophorou LG, Olthoff JK, Van Brunt RJ (1997) Sulfur hexafluoride and the electric power industry [J]. IEEE Electr Insul Mag 13(5):20–24
2. Dervos CT, Vassiliou P (2000) Sulfur hexafluoride (SF_6): global environmental effects and toxic byproduct formation [J]. J Air Waste Manag Assoc 50(1):137–141
3. Fang X, Hu X, Janssens-Maenhout G et al (2013) Sulfur hexafluoride (SF_6) emission estimates for China: an inventory for 1990–2010 and a projection to 2020 [J]. Environ Sci Technol 47(8):3848–3855
4. Kieffel Y, Irwin T, Ponchon P et al (2016) Green gas to replace SF_6 in electrical grids [J]. IEEE Power Energ Mag 14(2):32–39
5. Reilly J, Prinn R, Harnisch J et al (1999) Multi-gas assessment of the Kyoto protocol [J]. Nature 401(6753):549–555
6. Zhou S, Teng F, Tong Q (2018) Mitigating Sulfur Hexafluoride (SF_6) emission from electrical equipment in China [J]. Sustainability 10(7):2402
7. Mead I. International energy outlook 2017[J]. US Energy Information Administration, 2017.
8. Nielsen OK, Plejdrup MS, Winther M, Report DNI et al (2020) Emission Inventories 1990–2018-Submitted under the United Nations framework convention on climate change and the Kyoto protocol [J]. Scientific Report from DCE 2020:900
9. Tsai CH, Shao JM (2008) Formation of fluorine for abating sulfur hexafluoride in an atmospheric-pressure plasma environment[J]. J Hazard Mater 157(1):201–206
10. Kashiwagi D, Takai A, Takubo T et al (2009) Catalytic activity of rare earth phosphates for SF_6 decomposition and promotion effects of rare earths added into $AlPO_4$[J]. J Colloid Interface Sci 332(1):136–144
11. Zhang J, Zhou JZ, Liu Q et al (2013) Efficient removal of sulfur hexafluoride (SF_6) through reacting with recycled electroplating sludge [J]. Environ Sci Technol 47(12):6493–6499
12. Holze P, Horn B, Limberg C et al (2014) The activation of sulfur hexafluoride at highly reduced low-coordinate nickel dinitrogen complexes [J]. Angew Chem Int Ed 53(10):2750–2753
13. Song X, Liu X, Ye Z et al (2009) Photodegradation of SF_6 on polyisoprene surface: Implication on elimination of toxic byproducts [J]. J Hazard Mater 168(1):493–500
14. Govindan M, Gopal RA, Moon IS (2020) Electrochemical sequential reduction and oxidation facilitates the continual ambient temperature degradation of SF_6 to nontoxic gaseous compounds [J]. Chem Eng J 382:122881
15. Zhang X, Xiao H, Tang J et al (2017) Recent advances in decomposition of the most potent greenhouse gas SF_6[J]. Crit Rev Environ Sci Technol 47(18):1763–1782
16. Lee H, Chang M, Wu K (2004) Abatement of sulfur hexafluoride emissions from the semiconductor manufacturing process by atmospheric-pressure plasmas [J]. J Air Waste Manag Assoc 54(8):960–970
17. Zhang X, Xiao H, Hu X et al (2018) Effects of reduced electric field on sulfur hexafluoride removal for a double dielectric barrier discharge reactor [J]. IEEE Trans Plasma Sci 46(3):563–570
18. Radoiu M, Hussain S (2009) Microwave plasma removal of sulphur hexafluoride [J]. J Hazard Mater 164(1):39–45
19. Kim J, Cho C, Shin D et al (2015) Abatement of fluorinated compounds using a 2.45 GHz microwave plasma torch with a reverse vortex plasma reactor [J]. J Hazardous Mater 294:41–46
20. Shih M, Lee W, Tsai C et al (2002) Decomposition of SF_6 in an RF plasma environment [J]. J Air Waste Manag Assoc 52(11):1274–1280
21. Zhang X, Cui Z, Li Y et al (2018) Abatement of SF_6 in the presence of NH_3 by dielectric barrier discharge plasma[J]. J Hazard Mater 360:341–348
22. Cui Z, Zhang X, Yuan T et al (2019) Plasma-assisted abatement of SF_6 in a dielectric barrier discharge reactor: investigation of the effect of packing materials[J]. J Phys D Appl Phys 53(2):025205
23. Cui Z, Zhou C, Jafarzadeh A, et al. (2022) SF_6 catalytic degradation in a γ-Al_2O_3 packed bed plasma system: a combined experimental and theoretical study [J]. High Voltage. 7(6):1048–1058

24. Bogaerts A, Tu X, Whitehead J et al (2020) The 2020 plasma catalysis roadmap [J]. J Phys D Appl Phys 53(44):443001
25. Peri JB (1965) Infrared and gravimetric study of the surface hydration of γ-alumina[J]. J Phys Chem 69(1):211–219
26. Lefevre G, Duc M, Lepeut P et al (2002) Hydration of γ-alumina in water and its effects on surface reactivity[J]. Langmuir 18(20):7530–7537
27. Fernandez EM, Eglitis RI, Borstel G et al (2007) Ab initio calculations of H_2O and O_2 adsorption on Al_2O_3 substrates[J]. Comput Mater Sci 39(3):587–592
28. Butterworth T, Elder R, Allen R (2016) Effects of particle size on CO_2 reduction and discharge characteristics in a packed bed plasma reactor[J]. Chem Eng J 293:55–67
29. Wang X, Gao Y, Zhang S et al (2019) Nanosecond pulsed plasma assisted dry reforming of CH_4: the effect of plasma operating parameters[J]. Appl Energy 243:132–144
30. Jiang N, Guo L, Qiu C et al (2018) Reactive species distribution characteristics and toluene destruction in the three-electrode DBD reactor energized by different pulsed modes[J]. Chem Eng J 350:12–19
31. Neyts EC, Ostrikov K, Sunkara MK et al (2015) Plasma catalysis: synergistic effects at the nanoscale[J]. Chem Rev 115(24):13408–13446
32. Yi Y, Wang X, Jafarzadeh A et al (2021) Plasma-catalytic ammonia reforming of methane over cu-based catalysts for the production of HCN and H_2 at reduced temperature[J]. ACS Catal 11(3):1765–1773
33. Bal KM, Huygh S, Bogaerts A et al (2018) Effect of plasma-induced surface charging on catalytic processes: application to CO_2 activation[J]. Plasma Sourc Sci Technol 27(2):024001
34. Shirazi M, Neyts EC, Bogaerts A (2017) DFT study of Ni-catalyzed plasma dry reforming of methane[J]. Appl Catal B 205:605–614
35. Hutter J, Iannuzzi M, Schiffmann F et al (2014) cp2k: atomistic simulations of condensed matter systems [J]. Wiley Interdiscipl Rev: Comput Mol Sci 4(1):15–25
36. VandeVondele J, Krack M, Mohamed F et al (2005) Quickstep: Fast and accurate density functional calculations using a mixed Gaussian and plane waves approach [J]. Comput Phys Commun 167(2):103–128
37. VandeVondele J, Hutter J (2007) Gaussian basis sets for accurate calculations on molecular systems in gas and condensed phases [J]. J Chem Phys 127(11):114105
38. Goedecker S, Teter M, Hutter J (1996) Separable dual-space Gaussian pseudopotentials [J]. Phys Rev B 54(3):1703
39. Perdew J, Burke K, Ernzerhof M (1996) Generalized gradient approximation made simple [J]. Phys Rev Lett 77(18):3865
40. Grimme S, Antony J, Ehrlich S et al (2010) A consistent and accurate ab initio parametrization of density functional dispersion correction (DFT-D) for the 94 elements H-Pu [J]. J Chem Phys 132(15):154104
41. Head J, Zerner M (1985) A Broyden—Fletcher—Goldfarb—Shanno optimization procedure for molecular geometries [J]. Chem Phys Lett 122(3):264–270
42. Henkelman G, Uberuaga BP, Jónsson H (2000) A climbing image nudged elastic band method for finding saddle points and minimum energy paths [J]. J Chem Phys 113(22):9901–9904
43. Henkelman G, Arnaldsson A, Jónsson H (2006) A fast and robust algorithm for Bader decomposition of charge density [J]. Comput Mater Sci 36(3):354–360
44. Digne M, Sautet P, Raybaud P et al (2004) Use of DFT to achieve a rational understanding of acid–basic properties of γ-alumina surfaces [J]. J Catal 226(1):54–68
45. Wischert R, Laurent P, Copéret C et al (2012) γ-Alumina: the essential and unexpected role of water for the structure, stability, and reactivity of “defect” sites [J]. J Am Chem Soc 134(35):14430–14449
46. Martyna G, Tuckerman M (1999) A reciprocal space based method for treating long range interactions in ab initio and force-field-based calculations in clusters [J]. J Chem Phys 110(6):2810–2821
47. Jafarzadeh A, Bal K, Bogaerts A et al (2020) Activation of CO_2 on copper surfaces: the synergy between electric field, surface morphology, and excess electrons [J]. J Phys Chem C 124(12):6747–6755
48. Peeters FJJ, Van de Sanden MCM (2014) The influence of partial surface discharging on the electrical characterization of DBDs[J]. Plasma Sourc Sci Technol 24(1):015016
49. Butterworth T, Allen RWK (2017) Plasma-catalyst interaction studied in a single bead DBD reactor: dielectric constant effect on plasma dynamics[J]. Plasma Sourc Sci Technol 26(6):065008
50. Wang Q, Zhou X, Dai D et al (2021) Nonlinear feature in the spatial uniformity of an atmospheric helium dielectric barrier discharge with the inter-dielectric gap width enlarged [J]. Plasma Sour Sci Technol 30(5):56

51. Tsai WT (2007) The decomposition products of sulfur hexafluoride (SF_6): reviews of environmental and health risk analysis[J]. J Fluorine Chem 128(11):1345–1352
52. Zhang X, Cui Z, Li Y et al (2018) Study on degradation of SF_6 in the presence of H_2O and O_2 using dielectric barrier discharge[J]. IEEE Access 6:72748–72756
53. Zhang X, Yuan T, Cui Zhaolun et al (2020) Plasma-assisted abatement of SF_6 in a packed bed plasma reactor: understanding the effect of gas composition[J]. Plasma Sci Technol 22(5):055502
54. Tian Y, Zhang X, Tang B et al (2019) SF_6 abatement in a packed bed plasma reactor: study towards the effect of O_2 concentration[J]. RSC Adv 9(60):34827–34836
55. Xiao H, Zhang X, Hu X et al (2017) Experimental and simulation analysis on by-products of treatment of SF_6 using dielectric barrier discharge[J]. IEEE Trans Dielectr Electr Insul 24(3):1617–1624
56. Wang W, Kim H, Van Laer K et al (2018) Streamer propagation in a packed bed plasma reactor for plasma catalysis applications [J]. Chem Eng J 334:2467–2479
57. Deshlahra P, Wolf EE, Schneider WF (2009) A periodic density functional theory analysis of CO chemisorption on Pt (111) in the presence of uniform electric fields[J]. J Phys Chem A 113(16):4125–4133
58. Zhang QZ, Bogaerts A (2018) Propagation of a plasma streamer in catalyst pores[J]. Plasma Sources Sci Technol 27(3):035009
59. Cui Z, Meng S, Yi Y et al (2022) Plasma-catalytic methanol synthesis from CO_2 hydrogenation over a supported Cu cluster catalyst: insights into the reaction mechanism[J]. ACS Catal 12(2):1326–1337

Authors and Affiliations

Zhaolun Cui[1,2] · Chang Zhou[3] · Amin Jafarzadeh[2] · Xiaoxing Zhang[3] · Yanpeng Hao[1] · Licheng Li[1] · Annemie Bogaerts[2]

Xiaoxing Zhang
xiaoxingzhang@outlook.com

Annemie Bogaerts
annemie.bogaerts@uantwerpen.be

[1] School of Electric Power Engineering, South China University of Technology, Guangzhou 510630, China

[2] Department of Chemistry, Research Group PLASMANT, University of Antwerp, Universiteitsplein 1, 2610 Wilrijk-Antwerp, Belgium

[3] School of Electrical and Electronic Engineering, Hubei University of Technology, Wuhan 430068, China